ISSN 0038-0946, Solar System Research, 2023, Vol. 57, No. 5, pp. 449–466. © The Author(s), 2023. This article is an open access publication.
Russian Text © The Author(s), 2023, published in Astronomicheskii Vestnik, 2023, Vol. 57, No. 5, pp. 439–457.

# Search for Signs of Sublimation-Driven Dust Activity of Primitive-Type Asteroids Near Perihelion

**V. V. Busarev[a, b, *], E. V. Petrova[c], M. P. Shcherbina[a, b], S. Yu. Kuznetsov[d], M. A. Burlak[a], N. P. Ikonnikova[a], A. A. Savelova[e], and A. A. Belinskii[a]**

[a] *Sternberg Astronomical Institute, Moscow State University, Moscow, 119992 Russia*
[b] *Institute of Astronomy, Russian Academy of Sciences, Moscow, 119017 Russia*
[c] *Space Research Institute, Russian Academy of Sciences, Moscow, 117997 Russia*
[d] *Department of Space Research, Moscow State University, Moscow, 119992 Russia*
[e] *Department of Physics, Moscow State University, Moscow, 119992 Russia*
*****e-mail: busarev@sai.msu.ru*

Received February 27, 2023; revised March 30, 2023; accepted April 28, 2023

**Abstract**—In December 2021 to February 2022, the UBVRI photometry of 29 primitive-type asteroids of the Main Belt, being near the perihelion distances, was carried out at the 0.6-meter RC600 semiautomatic telescope of the Caucasus Mountain Observatory (CMO) of the Sternberg Astronomical Institute, Moscow State University. These observations, as well as the data processing and analysis, were aimed at searching for supposed sublimation-driven dust activity on asteroids under maximal subsolar temperatures. Among the tasks to be accomplished was the comparison of the physical and dynamic parameters of active and inactive asteroids. The main result is that substantial spectral signs of quasi-simultaneous sublimation-driven dust activity were detected on six primitive-type asteroids of the Main Belt—145 Adeona, 302 Clarissa, 322 Phaeo, 435 Ella, 690 Wratislavia, and 779 Nina (on 302 Clarissa, 322 Phaeo, 435 Ella, and 690 Wratislavia—for the first time). These six asteroids represent ~21% of all bodies included in the observation program. Probable spectral manifestations of activity at a lower intensity level were detected for the first time on five more asteroids—424 Gratia, 751 Faina, 762 Pulcova, 778 Theobalda, and 859 Bouzaréah. On 145 Adeona and 779 Nina, sublimation-driven dust activity near perihelion was registered for the third time for the last ten years; this time interval corresponds to about three orbital periods of these asteroids around the Sun. We consider the circumstances due to which five of the listed asteroids possess families. General processes and conditions that could and/or can influence the portion of primitive-type asteroids that quasi-simultaneously show signs of sublimation-driven dust activity are discussed.

**Keywords:** asteroids, UBVRI photometry, chemical and mineralogical composition, $H_2O$ and $CO_2$ ices, sublimation-driven dust activity

**DOI:** 10.1134/S0038094623050015

## INTRODUCTION

The problem of asteroid activity arose about 25 years ago, when several small objects, which showed signs of temporary comet-like activity, were discovered in the Main Asteroid Belt (MAB). In directly obtained images of these bodies, characteristic comet tails were found; because of this, these objects were called "Main Belt comets" (Hsieh and Jewitt, 2006; Hsieh, 2009). Then, it was suggested that these bodies might be nuclei of comets of Jupiter's family that lost activity and were trapped in the MAB under the influence of gravitational resonances (Hsieh and Haghighipour, 2016). However, despite careful searches, the total number of bodies that demonstrated clear signs of comet-like activity at the time of detection does not yet exceed ten, while the remaining two or three dozen, manifesting weaker signs of activity, are known asteroids of the Main Belt (see, e.g., Chandler et al., 2018; Hsieh et al., 2018; Jewitt and Hsieh, 2022). In this connection, it should be emphasized that the most numerous population of asteroids of the Main Belt (constituting, according to some estimates, up to ~75% of its members), are bodies of primitive types characterized by low-temperature mineralogy. They mainly belong to taxonomic (spectral) classes C, B, F, and G, which are believed to correspond to carbonaceous chondrites demonstrating the signs of aqueous alterations. Analyses of the spectral characteristics of these asteroids and their mineralogy (see, e.g., Gaffey et al., 1989, 2002), simulations of their formation processes (see, e.g., Zolensky et al., 1989; McSween Jr. et al., 2002), and studies of carbonaceous chondrites (see, e.g., Bradley, 2006; Alexander et al., 2018 and references therein) suggest that their parent bodies

were formed in the vicinity of the "$H_2O$ ice line" or beyond it in the early Solar System. Consequently, it is very likely that most of the Main Belt asteroids of the listed primitive types could potentially exhibit sublimation-driven dust activity (SDA), provided there are ice deposits in their interior. We will dwell on this issue at length in the Discussion section.

As shown by recent space-borne studies of the C-type asteroid 1 Ceres and 162173 Ryugu performed onboard the *Dawn* (NASA) and *Hayabusa 2* spacecraft, respectively (see, e.g., Schorghofer, 2016; Sugita et al., 2019), the regolith of primitive asteroids, consisting of very small particles, is highly porous, has extremely low thermal conductivity, and may reach several meters or even more in thickness. In this case, the "survival time" for ice (it is mostly $H_2O$ ice due to the higher volatility of $CO_2$) (see, e.g., Fanale and Salvail, 1989; Longhi, 2005)) may reach ~4 Gyr (Schorghofer, 2008, 2016). It may also be supposed that, on the surface of such asteroids, local subsurface ice deposits outcrop or ice materials are regularly ejected due to impact events occurring very often in the MAB in a wide energy range. The main indication of regular and massive impact events in the MAB is the persistent dust belts associated with it, which were found from the Infrared Astronomical Satellite (IRAS) data (Sykes et al., 1989; Veeder and Tedesco, 1992). The high probability of impact events in the MAB is also confirmed by the results of recent model calculations (Shustov et al., 2022). One more regular and widespread factor influencing asteroids is solar activity in the flare (in the electromagnetic range, most often in the X-ray range) and eruptive (ejections of the plasma substance) forms, which leads to the formation of shock magnetogasodynamic (MGD) waves in the solar wind. These waves can tear away the smallest electrified regolith particles from the surface of asteroids, set them in motion, and form a dust exosphere from them. At the moments of shock wave passages, the exosphere takes the form of a short cometary tail elongated in the antisolar direction (Busarev, 2018; Busarev et al., 2021). Other processes resulting in dust activity of asteroids may also take place (see, e.g., Jewitt, 2012 and references therein), but they are more exotic and/or less probable.

About ten years ago (Busarev et al., 2015), we started to search for sublimation-driven dust activity (SDA; by this term we understand the formation of gas flows during the sublimation of water ice, which carry fine submicron dust away and form a tenuous dust exosphere held near the body by its gravity and possibly electrostatic and induced ekectromagnetic forces) on primitive-type asteroids of the Main Belt, which is connected with their low-temperature origin and the supposed presence of subsurface ice layers. The use of low-resolution spectrophotometry enabled the detection of SDA on four asteroids at a time: 145 Adeona, 704 Interamnia, 779 Nina, and 1474 Beira (Busarev et al., 2015, 2016). Subsequent observations (including those considered here) twice confirmed SDA near perihelion on 145 Adeona, 779 Nina, and, repeatedly, on 704 Interamnia (Busarev et al., 2015, 2018; Busarev et al., 2019). Thus, there are indications of SDA that is periodic near perihelion and/or has long duration on some primitive asteroids, on the surface of which ice materials may outcrop probably because they are close to the surface. The purpose of this paper is to present and discuss the results of searching for new objects with signs of SDA among primitive-type asteroids of the Main Belt, as well as to study the causes of SDA.

## OBSERVATIONAL DATA AND THEIR ANALYSIS

We carried out new UBVRI observations of 29 primitive-type Main-Belt asteroids near perihelion in the period December 2021 to February 2022. We used the 0.6-meter RC600 telescope of the Caucasus Mountain Observatory (CMO) of the Sternberg Astronomical Institute (SAI) of Lomonosov Moscow State University (at an altitude of 2112 m above sea level). The telescope operates in semiautomatic mode and is equipped with the Andor photometer (iKON-L DZ-936N-BV; 2048 × 2048 CCD elements; pixel size 13.5 μm) with a set of $UBVR_cI_c$ filters of the Johnson–Cousins system and a CCD matrix cooled down to −60°C. The effective wavelengths of the $UBVR_cI_c$ filters, 355.9, 427.0, 543.9, 656.6, and 804.1 nm, respectively, were determined with the integral formula for the weighted average $\lambda_{eff}$ with the spectral transmission function $R(\lambda)$ for each of the filters (see, e.g., Bessell, 2005; Mironov, 2008):

$$\lambda_{eff} = \frac{\int R(\lambda)\lambda d\lambda}{\int R(\lambda)d\lambda}. \quad (1)$$

Table 1 contains the halfwidths (FWHM) and the effective wavelengths of the $UBVR_cI_c$ filters installed on the RC600 telescope (Fig. 1a) and the same parameters calculated for the whole $U'B'V'R_c'I_c'$ photometric system (Fig. 1c), including the quantum efficiency (QE) of the CCD matrix (Fig. 1a), the transparency of the entrance window (EW) of the camera (Fig. 1a), and the model median spectral transparency (ST) of the atmosphere at the SAI CMO (Fig. 1b).

The ST was calculated by using a software package to model numerically the radiative transfer in the Earth's atmosphere (Kornilov et al., 2016) as a function of the observatory's altitude above sea level, seasonal atmospheric water vapor content, and some other parameters (Emde et al., 2016). As can be seen from Figs. 1b and 1c, the $R_c$ and $I_c$ photometric bands are influenced by strong telluric bands of $O_2$ (A-band) and $H_2O$ (Kurucz, 2005).

As follows from Table 1, the relative differences in the $UBVR_cI_c$ and $U'B'V'R_c'I_c'$ effective wavelengths are

**Table 1.** The effective wavelengths $\lambda_{eff}$ and the halfwidths $\Delta\lambda$ for the installed $UBVR_cI_c$ filters and the resulting $U'B'V'R'_cI'_c$, photometric system, as well as their relative differences

| Effective wavelengths and halfwidths, nm | $U$ | $B$ | $V$ | $R_c$ | $I_c$ |
|---|---|---|---|---|---|
| $\lambda_{eff}$ | 355.9 | 427.0 | 543.9 | 656.6 | 804.1 |
| $\Delta\lambda$ | 61.7 | 95.8 | 99.8 | 155.4 | 167.8 |
| | $U'$ | $B'$ | $V'$ | $R'_c$ | $I'_c$ |
| $\lambda'_{eff}$ | 366.3 | 436.5 | 544.8 | 653.5 | 797.1 |
| $\left\|\left(\lambda'_{eff} - \lambda_{eff}\right)/\lambda_{eff}\right\|$ | 0.029 | 0.022 | 0.002 | 0.005 | 0.009 |
| $\Delta\lambda'$ | 42.9 | 89.3 | 100.3 | 153.7 | 163.4 |
| $\left\|(\Delta\lambda - \Delta\lambda')/\Delta\lambda\right\|$ | 0.305 | 0.068 | 0.005 | 0.011 | 0.026 |

0.029, 0.022, 0.002, 0.005, and 0.009, respectively, while the relative differences in the band halfwidths (FWHM) are 0.0305, 0.068, 0.005, 0.011, and 0.026, respectively. Since the latter are larger in magnitude, they may be taken as maximal errors in the measured intensities of light coming from the objects, when the intensity values are converted into the extra-atmospheric system.

Tables 2 and 3 contain a list of the 29 asteroids considered and their main physical, dynamic, and observational parameters. Table 3 also contains information on the solar-type stars used in the data processing.

### *Data Processing Technique*

To detect dust activity on asteroids, we used a technique based on the differential *UBVRI* photometry of these bodies and invariable standard solar-type stars for determining the reflectance of asteroids at effective wavelengths of the filters. It is commonly accepted in spectrophotometry that the reflectance (or the reflectance spectrum) of an asteroid, as an atmosphereless celestial body, is calculated by the following formula (see, e.g., Busarev, 1999):

$$\rho(\alpha,\lambda) = kI_a(\alpha,\lambda)\, p(\lambda)^{-\delta M} \big/ I_s(\lambda), \qquad (2)$$

where $I_a(\lambda)$ and $I_s(\lambda)$ are the monochromatic intensities of light registered at the receiver from the asteroid and the star standard, respectively (the latter is a solar analog, replacing the Sun in the first approximation), from which the sky background is removed; $\alpha$ is the phase angle of the asteroid; $p(\lambda)$ is the spectral transparency function of the Earth's atmosphere calculated for a given observational night; $\delta M = M_a - M_s$ is the difference in the air mass corresponding to the asteroid and the star standard; and $k$ is some constant factor.

In *UBVRI* photometry, in contrast to spectrophotometry, the integral intensities of light from objects in photometric bands, rather than in monochromatic ones, are used in formula (2). Besides, as already have been noted, the halfwidths of the photometric bands themselves and the values of $\lambda_{eff}$ (see Table 1) slightly changed under the influence of the spectral sensitivity of the CCD matrix and the spectral transparency function of the Earth's atmosphere (including the effects from telluric bands). However, since the intensity of light from the asteroid is divided by the similar quantity for a solar-type star (to determine the reflectance of the asteroid), these changes mutually compensate each other for the most part due to their multiplicative character. It is also important to emphasize that, during the observations, the air masses of the absolute majority of objects did not exceed 1.3, except for a few with air masses up to 1.5 (see Table 3). In addition, all of the discussed observations were carried out in winter, when the Earth's atmosphere in the vicinity of the SAI CMO was most transparent.

As can be seen from Table 3, the phase angles of asteroids at the moments of observations did not exceed 20° and, as follows from the results of laboratory model measurements (see, e.g., Sanchez et al., 2012), could not noticeably influence the shape of the approximated reflectance spectra. Consequently, to simplify the calculations with formula (2), it was assumed that $I_a(\alpha, \lambda) \approx I_a(\lambda)$ in the specified range of phase angles.

So, we were consistent with the following sequence of operations: (a) the uniformity of the sensitivity through the recording CCD is corrected (the flat field correction), as well as the dark currents and signal reading noises are taken into account; (b) the intensities of light from the asteroid and the nearest by coordinates G-type star, as a solar analog (the absence of

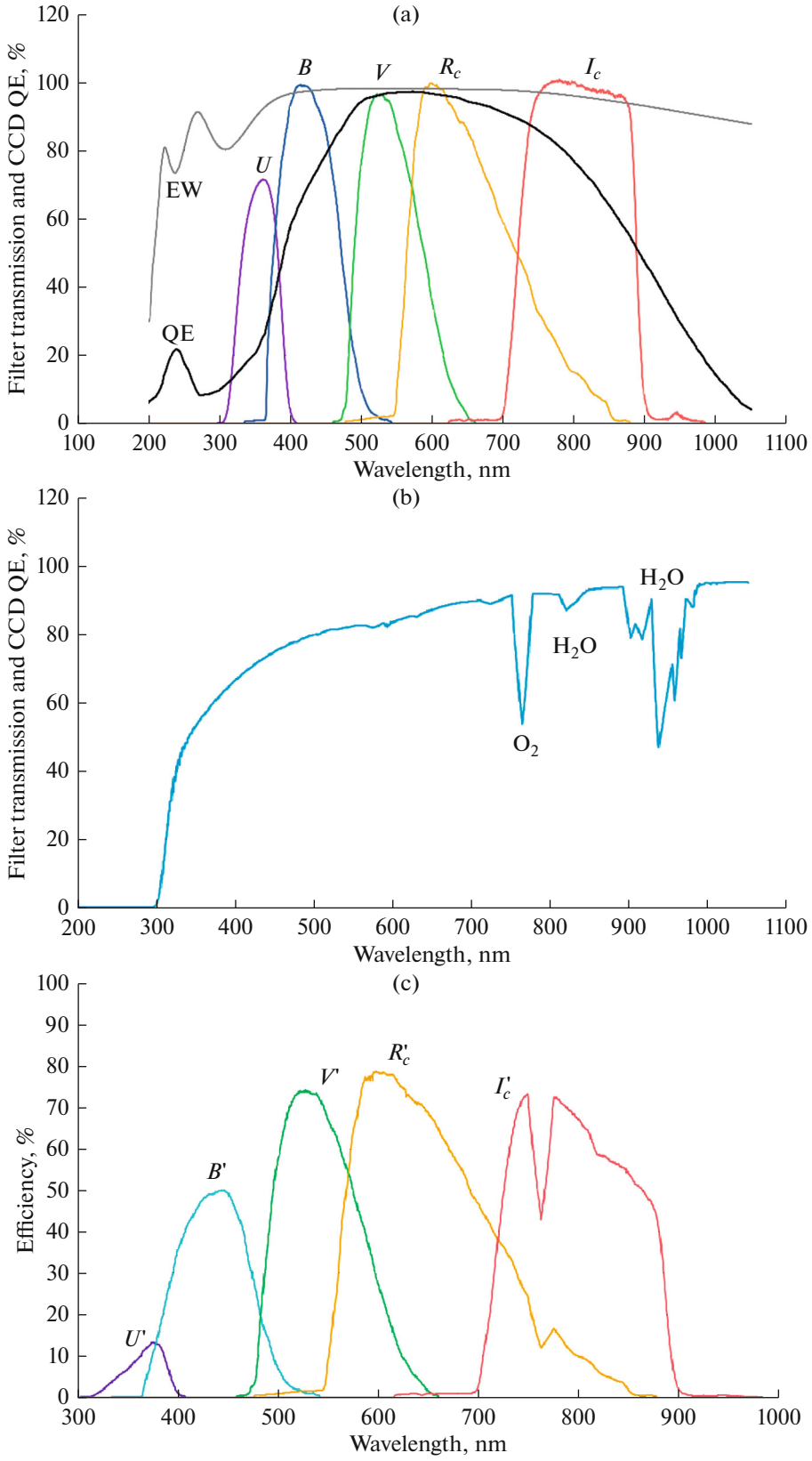


**Fig. 1.** Spectral characteristics of the photometer mounted at the RC600 telescope, the model spectral transparency (ST) of the terrestrial atmosphere at the CMO, and the whole photometric system: the spectral characteristics of the $UBVR_cI_c$ filters, the quantum efficiency (QE) of the CCD matrix, and the transparency of the entrance window (EW) of the camera (a); the median ST modeled (b); and the resulting spectral characteristics of the $U'B'V'R'_cI'_c$ photometric system used (c).

**Table 2.** Physical and dynamic parameters of the asteroids

| Number | Name | Tholen spectral class | SMASSII spectral class | Geometric albedo | Diameter, km | Semimajor axis (AU) | Orbit eccentricity | Perihelion distance (AU) | Family (name and number of members) |
|---|---|---|---|---|---|---|---|---|---|
| 91 | Aegina | CP | Ch | 0.048 | 103.402 | 2.590 | 0.107121 | 2.313 | – |
| 98 | Ianthe | CG | Ch | 0.029 | 132.788 | 2.688 | 0.187465 | 2.184 | – |
| 106 | Dione | G | Cgh | 0.044 | 207.869 | 3.180 | 0.159383 | 2.674 | – |
| 145 | ADEONA | C | Ch | 0.061 | 127.783 | 2.671 | 0.146710 | 2.280 | Adeona (6279) |
| 212 | Medea | DCX | – | 0.0465 | 136.12 | 3.116 | 0.102909 | 2.796 | – |
| 257 | Silesia | SCTU | Ch | 0 0545 | 72.66 | 3.118 | 0.112244 | 2.769 | – |
| 302 | CLARISSA | F | – | 0.0524 | 38.53 | 2.406 | 0.110197 | 2.141 | Clarissa (664) |
| 322 | PHAEO | X | X | 0.089 | 69.855 | 2.782 | 0.244701 | 2.101 | Phaeo (335) |
| 398 | Admete | – | C | 0.054 | 49.771 | 2.738 | 0.223934 | 2.125 | – |
| 424 | GRATIA | C | – | 0.027 | 102.565 | 2.774 | 0.109163 | 2.472 | – |
| 435 | ELLA | DCX | – | 0.118 | 34.792 | 2.449 | 0.154892 | 2.070 | – |
| 521 | Brixia | C | Ch | 0.073 | 107.227 | 2.743 | 0.278496 | 1.980 | – |
| 626 | Notburga | CX | Xc | 0.032 | 73.236 | 2.574 | 0.241884 | 1.952 | – |
| 659 | Nestor | XC | – | 0.035 | 112.320 | 5.166 | 0.116690 | 4.563 | |
| 690 | WRATISLAVIA | CPF | – | 0 0604 | 134.65 | 3.149 | 0.176809 | 2.592 | – |
| 705 | Erminia | X | C | 0.031 | 132.261 | 2.924 | 0.051088 | 2.775 | – |
| 751 | FAINA | C | Ch | 0.027 | 113.699 | 2.551 | 0.151115 | 2.166 | – |
| 762 | PULCOVA | F | – | 0.040 | 147.343 | 3.154 | 0.106967 | 2.818 | – |
| 778 | THEOBALDA | F | – | 0.079 | 55.317 | 3.179 | 0.256195 | 2.366 | Theobalda (3185) |
| 779 | NINA | – | X | 0 157 | 80.572 | 2.664 | 0.227025 | 2.059 | – |
| 859 | BOUZARÉAH | C | – | 0.031 | 65.417 | 3.226 | 0.110093 | 2.872 | – |
| 916 | America | C | – | 0.0530 | 33.23 | 2.365 | 0.236585 | 1.805 | – |
| 934 | Thüringia | – | Ch | 0.047 | 53.714 | 2.749 | 0.215947 | 2.156 | – |
| 1001 | Gaussia | PC | – | 0041 | 72.711 | 3.209 | 0.122298 | 2.818 | – |
| 1115 | Sabauda | C | – | 0.044 | 75.907 | 3.099 | 0.173958 | 2.561 | – |
| 1189 | Terentia | – | Ch | 0.042 | 59.246 | 2.931 | 0.111807 | 2.604 | Terentia (421) |
| 1235 | Schorria | CX | – | – | – | 1.910 | 0.154585 | 1.615 | – |
| 1295 | Deflotte | c | – | 0.046 | 47.407 | 3.390 | 0.124333 | 2.970 | – |
| 1448 | Lindbladia | CX | – | 0.0378 | 20.65 | 2.373 | 0.185703 | 1.932 | – |

The names of asteroids with detected SDA are capitalized and underlined; the names of asteroids suspected of activity are capitalized without underlining; the data in columns 3, 4, 5, 6, 7, 8, and 9 are taken from https://ssd.jpl.nasa.gov/; the data in column 10 are according to Novaković et al. (2022) (http://asteroids.matf.bg.ac.rs/fam/families/afp.fam.summary).

variability in this star was controlled according to databases), are sequentially registered in all filters; (c) the values of the spectral transparency function of the Earth's atmosphere $p(\lambda)$ are determined at the effective wavelengths of the filters by comparing the intensities of light from the star standard at two different air masses ($I_1(\lambda)$ and $I_2(\lambda)$ for $M1$ and $M2$, respectively):

$$p(\lambda) = [I_2(\lambda)/I_1(\lambda)]^{1/(M1-M2)}; \quad (3)$$

(d) the asteroid's reflectance at five effective wavelengths of the filters is calculated according to the standard formula (2) (it should be emphasized that this technique makes the value of the asteroid's reflectance to be independent of the influence of the Earth's atmosphere); (e) the asteroid's reflectance calculated in all filters is normalized to the value of this quantity in filter $V$; and finally, (f) with the use of these data, the curve that is a normalized approximated reflectance spectrum of the asteroid (hereafter, conventionally, "normalized reflectance spectrum" or NRS) is plotted.

Thus, for each night of the observations, we determined the average UBVRI values of the spectral transparency of the atmosphere with formula (3) using the measurements of standard solar-type stars. The short-term photometric stability (extinction) of the atmosphere at the moments of observations of asteroids was verified by the closest invariable stars (within the common CCD frames) by calculating and comparing three successive approximated spectra of each of these stars (see insets in Figs. 2, 3). From the coincidence of these spectra, we see that these errors are negligible.

One more important issue is the accuracy in the coincidence of the energy distributions in the spec-

**Table 3.** Parameters of observations of the asteroids and stars

| Date | Mean UT (h:m:s) | Geocentric distance (AU) | Heliocentric distance (AU) | Orbit inclination (deg) | Phase angle (deg) | *Magnitude* ($V^m$) | Asteroid's air mass | G-type star standard | Star's air mass |
|---|---|---|---|---|---|---|---|---|---|
| 91 Aegina | | | | | | | | | |
| Jan. 5, 2022 | 01:58:58 | 1.5880 | 2.3905 | 2.103 | 16.7797 | 12.691 | 1.245 | HD 107515 | 1.191 |
| Feb. 12, 2022 | 23:04:30 | 1.4389 | 2.4255 | | 1.0997 | 11.788 | 1.216 | HD 107515 | 1.209 |
| 98 Ianthe | | | | | | | | | |
| Feb. 25, 2022 | 23:34:58 | 1.2201 | 2.1846 | 15.576 | 7.8358 | 11.585 | 1.283 | HD 107515 | 1.188 |
| | 23:37:17 | 1.2201 | 2.1846 | | 7.8363 | 11.585 | 1.289 | | |
| | 23:41:53 | 1.2201 | 2.1846 | | 7.8375 | 11.585 | 1.306 | | |
| 106 Dione | | | | | | | | | |
| Dec. 16, 2021 16 | 22:39:07 | 1.8086 | 2.7732 | 4.576 | 4.9734 | 11.531 | 1.259 | Wolf 1059 | 1.052 |
| 145 ADEONA | | | | | | | | | |
| Dec. 10, 2021 | 20:28:32 | 1.5092 | 2.4338 | 12.62 | 10.1364 | 11.698 | 1.195 | Cl Melotte 201100 | 1.021 |
| 212 Medea | | | | | | | | | |
| Jan. 9, 2022 | 18:10:24 | 19886 | 2.8200 | 4.278 | 12.7261 | 12.886 | 1.047 | HD 287324 | 1.217 |
| 257 Silesia | | | | | | | | | |
| Dec. 12, 2021 | 0:05:33 | 1.8166 | 2.7883 | 3.613 | 4.0649 | 13.362 | 1.171 | Wolf 1059 | 1.038 |
| 302 CLARISSA | | | | | | | | | |
| Jan. 9, 2022 | 17:28:18 | 1.3144 | 2.1586 | 3.413 | 17.2185 | 14.314 | 1.060 | HD 287324 | 1.262 |
| | 17:35:01 | 1.3145 | 2.1586 | | 17.2204 | 14.314 | 1.055 | | |
| | 17:45:18 | 1.3145 | 2.1586 | | 17.2232 | 14.314 | 1 050 | | |
| 322 PHAEO | | | | | | | | | |
| Dec. 11, 2021 | 18:47:19 | 1.3911 | 2 3491 | 8.045 | 7.2219 | 12.210 | 1109 | Cl Melotte 201100 | 1.010 |
| 398 Admete | | | | | | | | | |
| Dec. 11, 2021 | 01:22:37 | 1.4185 | 2.1760 | 9.553 | 20.6427 | 13.897 | 1.154 | Wolf 1059 | 1.095 |
| Feb. 12, 2022 | 22:21:47 | 1.3427 | 2.2726 | | 10.8845 | 13.535 | 1.465 | HD 107515 | 1.289 |
| 424 GRATIA | | | | | | | | | |
| Jan. 6, 2022 | 02:33:23 | 1.8216 | 2.6087 | 8.221 | 15.5486 | 13.837 | 1.252 | HD 107515 | 1.183 |
| Feb. 12, 2022 | 23:48:46 | 1.6688 | 2.6480 | | 3.4263 | 13.159 | 1.216 | HD 107515 | 1.187 |
| 435 ELLA | | | | | | | | | |
| Dec. 7, 2021 | 20:53:15 | 1.3146 | 2.2377 | 1.816 | 11.5058 | 13.469 | 1.193 | HIP 14697 | 1.056 |
| | 20:57:42 | 1.3146 | 2.2377 | | 11.5071 | 13.469 | 1.200 | | |
| | 21:04:17 | 1.3146 | 2.2377 | | 11.5093 | 13.469 | 1.215 | | |

**Table 3.** (Contd.)

| Date | Mean UT (h:m:s) | Geocentric distance (AU) | Heliocentric distance (AU) | Orbit inclination (deg) | Phase angle (deg) | *Magnitude* ($V^m$) | Asteroid's air mass | G-type star standard | Star's air mass |
|---|---|---|---|---|---|---|---|---|---|
| 521 Brixia | | | | | | | | | |
| | 19:46:32 | 1.0598 | 2.0243 | 10.582 | 7.7593 | 10.899 | 1.142 | | |
| Dec. 11, 2021 | 19:47:59 | 1.0598 | 2.0243 | | 7.7600 | 10.899 | 1.141 | HD 285598 | 1.140 |
| | 19:50:11 | 1.0598 | 2.0243 | | 7.7607 | 10.899 | 1.141 | | |
| Dec. 16, 2021 | 20:18:38 | 1.0834 | 2.0311 | | 10.2520 | 11.093 | 1.146 | HD 287324 | 1.204 |
| 626 Notburga | | | | | | | | | |
| Dec. 7, 2021 | 18:58:39 | 1.2555 | 2 0434 | 25.378 | 21.2777 | 12.326 | 1.052 | BD + 40349 | 1.031 |
| 659 Nestor | | | | | | | | | |
| Dec 7, 2021 | 19:46:47 | 4.0861 | 4 9341 | 4.522 | 6.3949 | 15.713 | 1.133 | BD + 23331 | 1.102 |
| 690 WRATISLAVIA | | | | | | | | | |
| Dec. 10, 2021 | 20:03:14 | 18441 | 2.7692 | 11 244 | 8.5592 | 12.188 | 1 094 | Cl Melotte 201100 | 1.009 |
| 705 Erminia | | | | | | | | | |
| Jan. 9, 2022 | 03:00:46 | 1.9850 | 2.7850 | 25.018 | 13.9748 | 13.000 | 1.143 | HD 107515 | 1.200 |
| 51 FAINA | | | | | | | | | |
| Dec. 8, 2021 | 00:25:54 | 1.6802 | 2.4585 | 15.596 | 17.0965 | 12.840 | 1.031 | Wolf 1059 | 1.039 |
| | 23:09:01 | 1.7505 | 2.5730 | | 14.8028 | 12.942 | 1.467 | | |
| Feb. 15, 2022 | 23:12:34 | 1.7505 | 2.5730 | | 14.8034 | 12.942 | 1.481 | HD 107515 | 1.194 |
| | 23:17:48 | 1.7506 | 2.5730 | | 14.8044 | 12.942 | 1.506 | | |
| 762 PULCOVA | | | | | | | | | |
| Dec. 13, 2021 | 02:49:26 | 1.9890 | 2.8579 | 13.097 | 11.1502 | 12.536 | 1.338 | Wolf 1059 | 1.301 |
| | 21:27:58 | 2.1322 | 2.8272 | | 16.5050 | 12.856 | 1.521 | | |
| Feb. 25, 2022 | 21:32:25 | 2.1327 | 2.8272 | | 16.5056 | 12.856 | 1.544 | HD 107515 | 1.276 |
| | 21:39:00 | 2.1323 | 2.8272 | | 16.5067 | 12.856 | 1.585 | | |
| 778 THEOBALDA | | | | | | | | | |
| Dec. 7, 2021 | 23:51:43 | 1.5708 | 2.3682 | 13.711 | 17.2617 | 13.553 | 1.024 | Wolf 1059 | 1.038 |
| | 21:45:15 | 1.5671 | 2.4176 | | 14.8203 | 13.510 | 1.259 | | |
| Feb. 15, 2022 | 21:49:07 | 1.5671 | 2.4176 | | 14.8213 | 13.510 | 1.271 | HD 107515 | 1.334 |
| | 21:54:52 | 1.5672 | 2.4177 | | 14.8227 | 13.510 | 1.291 | | |
| 779 NINA | | | | | | | | | |
| | 20:24:41 | 1.6369 | 2.5728 | 14.574 | 8.5445 | 11.729 | 1.032 | | |
| Dec. 11, 2021 | 20:27:00 | 1.6369 | 2.5728 | | 8.5452 | 11.729 | 1.034 | Cl Melotte 201100 | 1.021 |
| | 20:30:35 | 1.6369 | 2.5728 | | 8.5459 | 11.729 | 1.036 | | |

**Table 3.** (Contd.)

| Date | Mean UT (h:m:s) | Geocentric distance (AU) | Heliocentric distance (AU) | Orbit inclination (deg) | Phase angle (deg) | *Magnitude* ($V^m$) | Asteroid's air mass | G-type star standard | Star's air mass |
|---|---|---|---|---|---|---|---|---|---|
| 859 BOUZARÉAH | | | | | | | | | |
| Dec. 29, 2021 | 23:41:04 | 2.2239 | 3 0467 | 13.503 | 11.8857 | 14.655 | 1.017 | Wolf 1059 | 1.064 |
| | 22:57:29 | 2.2636 | 3.1045 | | 11.3062 | 14.713 | 1.286 | | |
| Feb. 25, 2022 | 23:02:06 | 2.2636 | 3.1045 | | 11.3070 | 14.713 | 1.303 | HD 107515 | 1.183 |
| | 23:09:05 | 2.2637 | 3.1045 | | 11.3082 | 14.713 | 1.327 | | |
| 916 America | | | | | | | | | |
| Dec. 16, 2021 | 00:45:59 | 1.2611 | 2.1835 | 11.095 | 11.8812 | 14.440 | 1.079 | Wolf 1059 | 1.074 |
| 934 Thüringia | | | | | | | | | |
| Dec. 11, 2021 | 23:28:54 | 1.3752 | 2.3172 | 14.081 | 9.2141 | 13.241 | 1.081 | Wolf 1059 | 1.042 |
| 1001 Gaussia | | | | | | | | | |
| | 18:44:11 | 2.0539 | 2 8823 | 9.315 | 12.4951 | 14.365 | 1 084 | | |
| Jan. 9, 2022 | 18:51:01 | 2.0539 | 2.8823 | | 12.4966 | 14.365 | 1.086 | HD 287324 | 1.205 |
| | 19:01:16 | 2.0540 | 2.8823 | | 12.4987 | 14.365 | 1.091 | | |
| 1115 Sabauda | | | | | | | | | |
| Dec. 13, 2021 | 02:17:01 | 1.7179 | 2.6029 | 15.285 | 11.7168 | 13.716 | 1.221 | Wolf 1059 | 1.205 |
| 1189 Terentia | | | | | | | | | |
| Dec. 16, 2021 | 21:53:01 | 1.8022 | 2.7495 | 9.863 | 6.8655 | 13.998 | 1171 | Wolf 1059 | 1.103 |
| 1235 Schorria | | | | | | | | | |
| | 00:36:26 | 1.0017 | 1.7849 | 25.002 | 26.0165 | 15.646 | 1.365 | | |
| Feb. 16, 2022 | 00:43:56 | 1.0018 | 1.7849 | | 26.0170 | 15.646 | 1.383 | HD 107515 | 1.215 |
| | 00:54:59 | 1.0018 | 1.7849 | | 26.0178 | 15.646 | 1.416 | | |
| 1295 Deflotte | | | | | | | | | |
| | 20:13:07 | 2.0848 | 3 0410 | 2.886 | 5.6825 | 15.196 | 1.150 | | |
| Feb. 18, 2022 | 20:19:43 | 2.0848 | 3.0410 | | 5.6840 | 15.196 | 1.151 | Wolf 1059 | 1.066 |
| | 20:32:19 | 2 0848 | 3 0410 | | 5.6873 | 15.196 | 1.154 | | |
| 1448 Lindbladia | | | | | | | | | |
| | 22:23:03 | 1.0636 | 1.9350 | 5.813 | 18.6507 | 15.414 | 1.328 | | |
| Feb. 15, 2022 | 22:30:52 | 1.0636 | 1.9350 | | 18.6527 | 15.414 | 1.354 | HD 107515 | 1.246 |
| | 22:42:27 | 1.0636 | 1 9350 | | 18.6563 | 15.414 | 1.403 | | |

The names of asteroids with detected SDA are capitalized and underlined; the names of asteroids suspected of activity are capitalized without underlining.

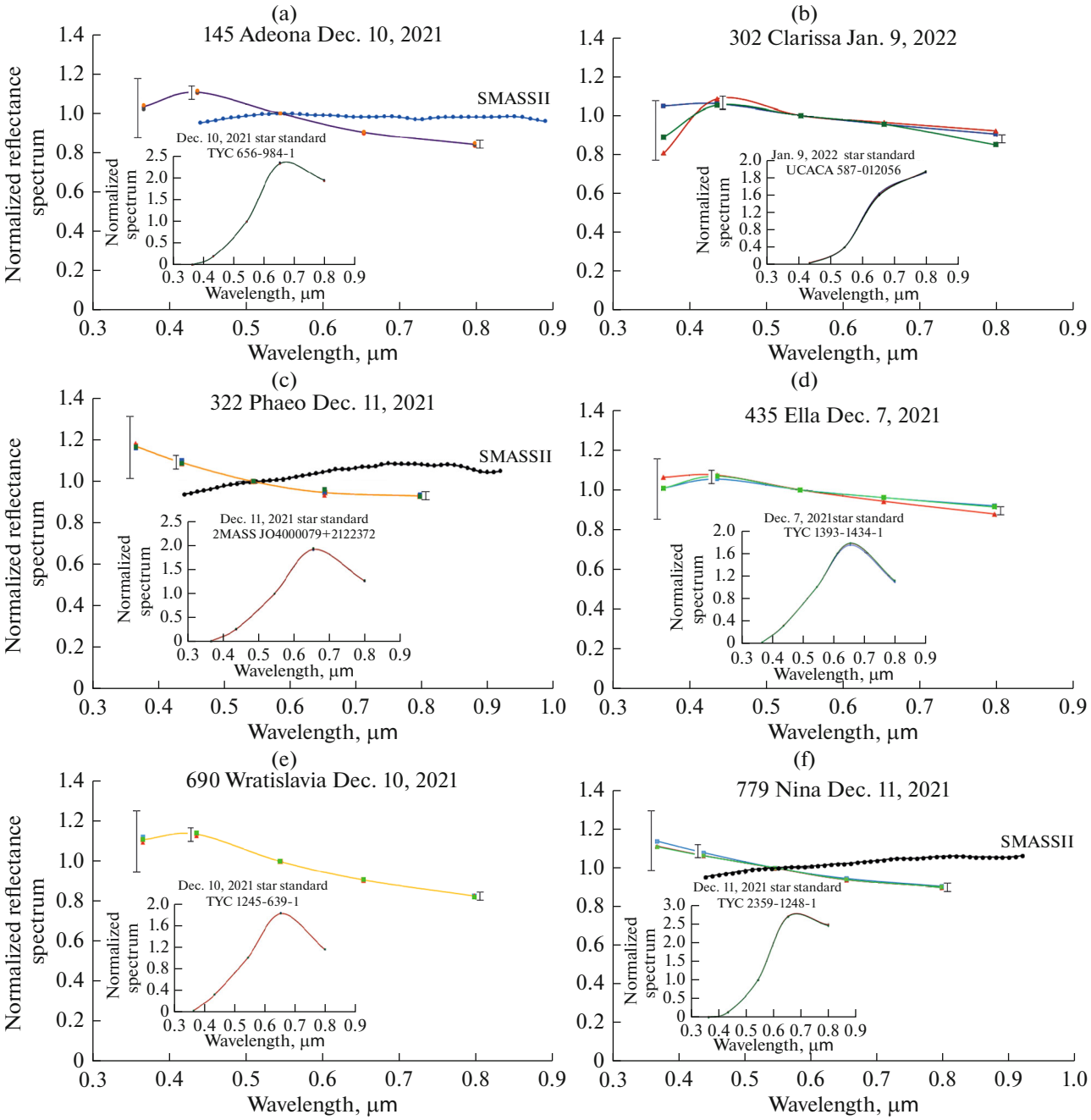


**Fig. 2.** The normalized approximated reflectance spectra of asteroids demonstrating clear signs of activity—145 Adeona (a), 302 Clarissa (b), 322 Phaeo (c), 435 Ella (d), 690 Wratislavia (e), and 779 Nina (f). The dates of observations are shown in the corresponding diagrams. In the diagrams for 145 Adeona, 322 Phaeo, and 779 Nina, the normalized reflectance spectra of these asteroids from the SMASSII database (https://sbnapps.psi.edu/ferret/SimpleSearch/results.action#Asteroid%20145%20AdeonaEAR-AI0028-4-SBN0001/SMASSII-V1.0) are shown for comparison. The latter were obtained under normal conditions (no signs of activity in the asteroids were observed). In the inserts, there are spectra of the star standards used to control the stability of the spectral transparency of the Earth's atmosphere and to estimate the overall accuracy of measurements. The maximal errors of measurements (derived by calculating the FWHM of bands in the $U'B'V'R'_cI'_c$ photometric system) are indicated for the $U'$, $B'$, and $I'_c$ photometric bands. For the $V'$ and $R'_c$ bands, the errors are not shown, since they are less than 1%.

trum of the Sun and G-type stars, which were used in the study to calculate the reflectance spectra of asteroids. Given the greatest informative value of the short-wavelength spectral range for searching for the signs of asteroid activity, we evaluated this accuracy by relative deviations of the B–V color indices of stars listed in Table 3 (according to the Simbad database, http://simbad.cds.unistra.fr/simbad/sim-fbasic) from

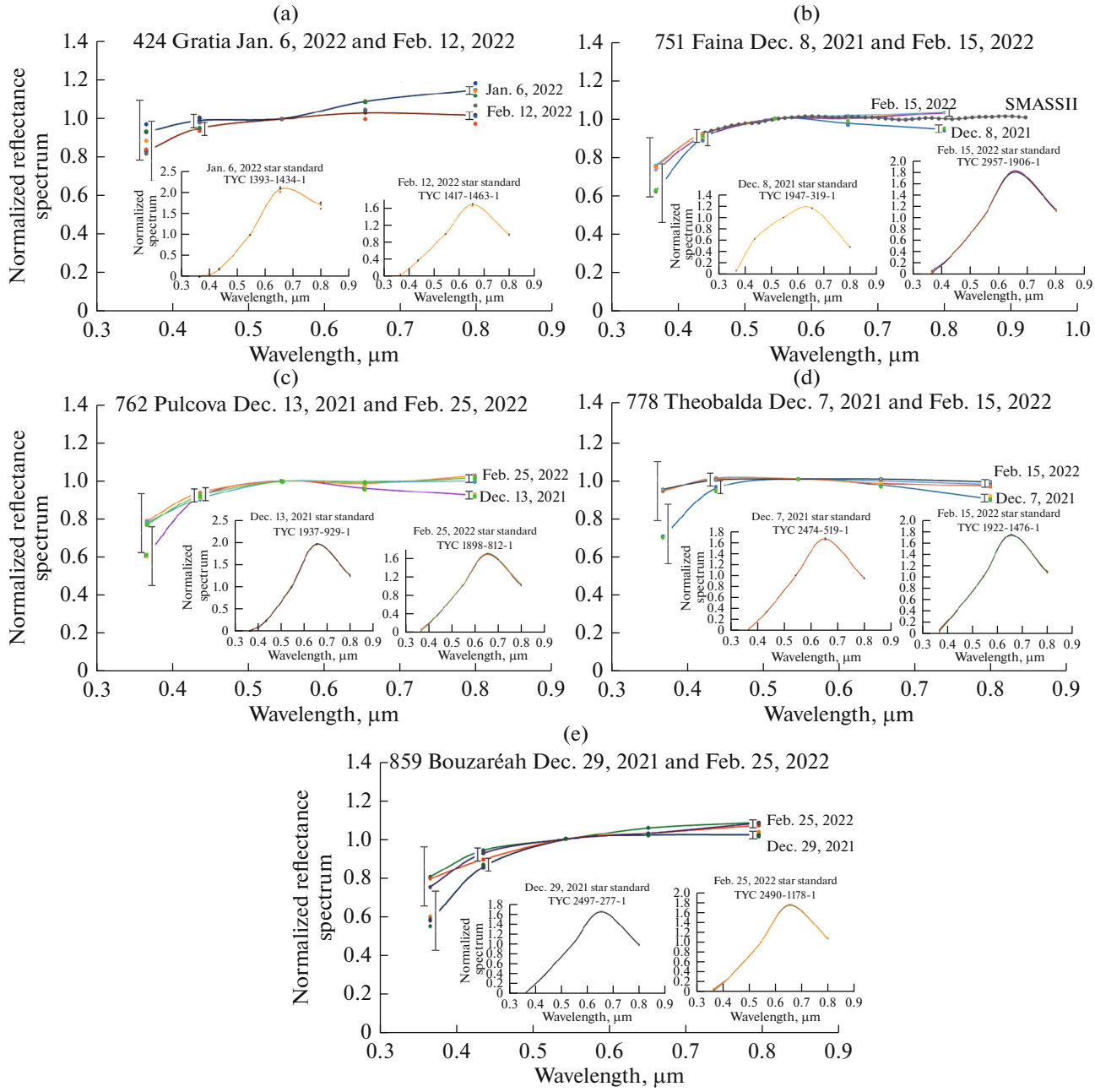


**Fig. 3.** The normalized approximated reflectance spectra of asteroids, for which probable (relatively weak) signs of activity were observed—424 Gratia (a), 751 Faina (b), 762 Pulcova (c), 778 Theobalda (d), and 859 Bouzaréah (e). The dates of observations are shown in the corresponding diagrams. In the diagram for 751 Faina, the normalized reflectance spectrum of the asteroid from the SMASSII database (https://sbnapps.psi.edu/ferret/SimpleSearch/results.action#Asteroid%20145%20AdeonaEAR-AI0028-4-SBN0001/SMASSII-V1.0) is shown for comparison. The latter was obtained under no signs of activity in the asteroid. In the inserts, there are spectra of the star standards, which were observed simultaneously with the asteroids and were used to control the stability of the spectral transparency of the Earth's atmosphere and to estimate the overall accuracy of measurements. The maximal errors of measurements (derived by calculating the FWHM of bands in the $U'B'V'R'_cI'_c$ photometric system) are indicated for the $U'$, $B'$, and $I'_c$ photometric bands. For the $V'$ and $R'_c$ bands, the errors are not shown, since they are less than 1%.

the solar color index (0.65). The calculations showed that the specified errors in calculating the NRS of asteroids demonstrating obvious signs of activity and those suspected of activity do not go beyond a range of 1–3%.

*Results of Observations and Their Interpretation*

The main physical and dynamic parameters of the asteroids are listed in Table 2, while the parameters of observations of all these objects are in Table 3.

The normalized approximated reflectance spectra (NRS) of asteroids 145 Adeona, 302 Clarissa, 322 Phaeo, 435 Ella, 690 Wratislavia, and 779 Nina, which show clear signs of activity, are presented in Fig. 2, while the NRS of asteroids 424 Gratia, 751 Faina, 762 Pulcova, 778 Theobalda, and 859 Bouzaréah, which are suspected of activity or show weaker signs of activity, are in Fig. 3.

In order to further choose more preferable of two possible variants of measurements (serial or individual), the illuminance from an asteroid registered on the receiver was measured in one of two following ways. (1) We considered the data obtained in three successive series, in each of which the measurements in all filters were taken sequentially once, while the data obtained were not averaged. (2) We considered three measurements in each of the filters sequentially in all filters, and the data in each filter were averaged. The differences in the order of measurements led to somewhat different representations of the results in the diagrams (see Figs. 2, 3). In the first case, the serial data, which are marked by points of the same color in the diagrams, were used to construct three separate NRSs. In the second case, the three measurements in each of the filters were averaged, and only one NRS was plotted according to the averages derived. Thus, for each of the asteroids on the corresponding date, either three consecutive approximated spectra (for serial measurements) or one averaged NRS (for individual measurements) are plotted. Based on a comparison of the two calculation variants and the representation of the observational data in many bands, we conclude that the method of serial measurements is preferable, since its usage makes it possible to extract from the resulting diagrams more information about the evolution of the spectral features of active asteroids rather than only about the feature's shape. As was shown in the previous papers (see, e.g., Busarev et al., 2021, 2022), these spectral features characterize the composition and structure of dust particles in the exospheres of active asteroids.

The insets in each of the diagrams (see Figs. 2, 3) also show three normalized approximated spectra of one or two (in repeated observations of some asteroids) star standards, which were used to control the stability of the spectral transparency of the Earth's atmosphere. However, we can see that in most cases the spectra of each of these stars, highlighted by different colors, merge into a single spectrum, which demonstrates good observational conditions. The close coincidence of the approximated spectra of star standards characterizes the high accuracy of measurements and calculations of the NRSs of the considered asteroids in general.

As follows from Fig. 2, in the NRSs of asteroids 145 Adeona, 302 Clarissa, 322 Phaeo, 435 Ella, 690 Wratislavia, and 779 Nina, the deviations from the standard spectral characteristics, the SMASSII spectra (if available), were observed for one night. These deviations reached ~30 and ~20% in the U and B bands, respectively. Though the errors in the SMASSII data are not available (nor are the phase angles) (https://sbnapps.psi.edu/ferret/SimpleSearch/results.action#Asteroid%20145%20AdeonaEAR-A-I0028-4-SBN0001/SMASSII-V1.0), in the original papers (see, e.g., Bus, Binzel, 2002), the relative accuracy of the CCD data is generally accepted at ~1–2% in the visible spectrum range and up to ~3–4% near the short- and long-wavelength boundaries, while the phase angles do not exceed 20°–30°. Unfortunately, in the SMASSII data available, the short-wavelength boundary is near ~0.44 μm. We may argue that, in the data we obtained in the $V'$, $R_c'$, and $I_c'$ bands, a similar or even higher accuracy was achieved (see Table 1). At the same time, in the B' band, the deviations considered in the spectra of active asteroids are an order of magnitude larger than the maximal errors derived from probable changes in the band halfwidth, while in the U' band, they are comparable to these values. The largest measurement errors (obtained by calculating the FWHM of the bands in the $U'B'V'R_c'I_c'$ photometric system) are shown in Figs. 2 and 3 for photometric bands $U'$ (31%), $B'$ (7%), and $I_c'$ (3%). For bands $V'$ and $R_c'$, the errors are not shown in the figures, since they are less than 1%.

For asteroids 302 Clarissa, 435 Ella, and 690 Wratislavia, the SMASSII data are absent, but negative gradients of their NRSs are identical to those observed for asteroids 145, 322, and 779. We interpret the mentioned features as clear signs of SDA and the presence of a dust exosphere on all six asteroids. A common spectral detail in the NRSs of 145 Adeona, 302 Clarissa, 435 Ella, and 690 Wratislavia is the light-scattering maximum at wavelengths within 0.44–0.46 μm (Fig. 2).

For asteroids with less pronounced signs of activity, or yet "suspected of activity," the differences in the NRS (when comparing the data for two arbitrary nights) reached ~15–20%; moreover, they were more significant in the short-wavelength spectral range (Fig. 3). Since in this group of asteroids the SMASSII data are available only for 751 Faina (see Fig. 3b), we used the averaged normalized spectra, characterizing the taxonomic classes of these asteroids (Tholen, Barucci, 1989) according to Tholen's classification (Tholen, 1989), as standard (Table 2). In the group of objects under consideration, we should pay attention to the SDA signs on asteroid 424 Gratia, which can be judged by the overall scatter of points in its NRS and the simultaneous absence of such an effect in the spectra of the reference stars shown in the insets (Fig. 3a). Moreover, in the NRS of Gratia obtained on January 6, 2022, there are two faint light-scattering maxima at 0.44 and 0.64 μm (Fig. 3a), similar in position to more pronounced spectral details found earlier in the NRSs of the other active asteroids (Busarev et al., 2016, 2019;

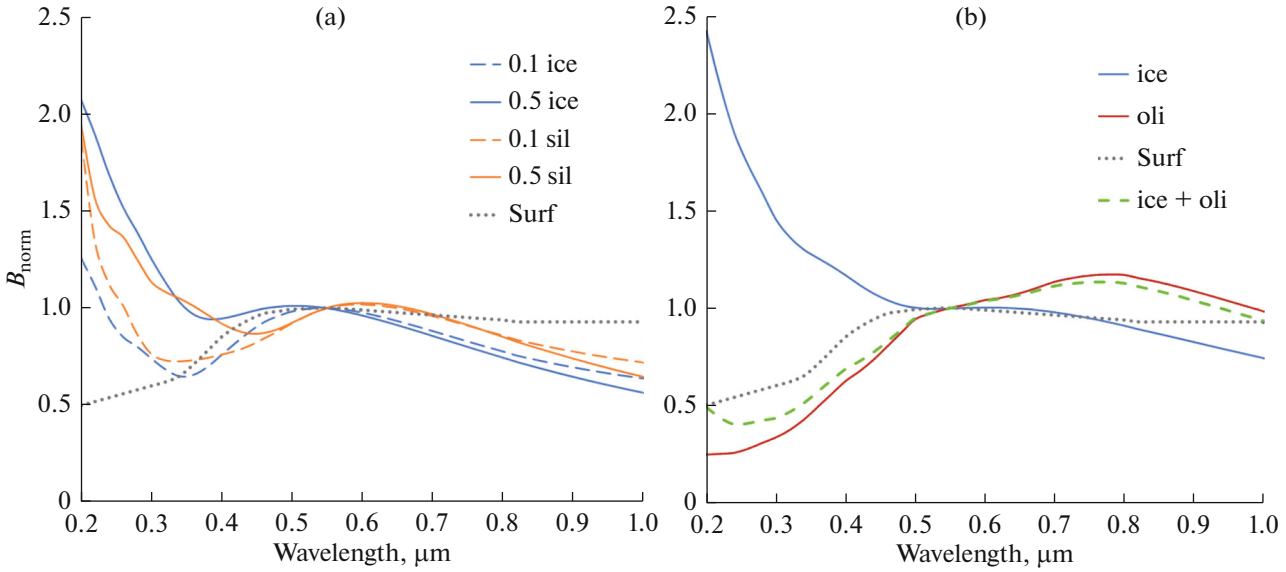


**Fig. 4.** The reflectance spectra $B_{norm}$ of a conventional low-albedo (0.07) asteroid of the C type observed at a phase angle of 10°. The asteroid is enveloped by a dust exosphere containing spherical particles with the composition indicated. Their sizes are specified by $R_{eff} = 0.1$ μm under $\nu_{eff} = 0.02$ and $\tau = 0.1$ or 0.5 for $H_2O$ ice (ice) and astronomical silicates (sil) (a) and under $\nu_{eff} = 0.10$ and $\tau = 0.5$ for ice and olivines (oli) (b). The assumed spectrum of the asteroid's surface is shown with the curve "Surf."

Busarev et al., 2021), which can be considered as additional evidence that the asteroid possesses a rarefied dust exosphere. As shown by numerical simulations of the light scattering on particles of complex structure, these details may appear due to the interference of light scattered on submicron components of such particles in the exosphere (Busarev et al., 2021; Petrova and Busarev, 2023). At the same time, it is natural to expect that very small particles, smaller than the wavelength, are carried out into the exosphere first. Their contribution to the intensity of scattered light should significantly grow with decreasing the wavelength (as well as the contribution of the gas component, but the latter is relatively small (Bockelée-Morvan et al., 2016)), which may change a typical positive gradient for the NRS of the considered asteroids into a negative one. We observe exactly such changes in the spectra presented in Figs. 2 and 3.

In Fig. 4, we show examples of the model reflectance spectra $B_{norm}$ (normalized to the value at a wavelength of 0.55 μm) of a conventional low-albedo C-type asteroid enveloped by a dust exosphere with the optical depth $\tau$, which is composed of homogeneous polydisperse submicron particles with the effective radius $R_{eff}$ under the variance $\nu_{eff}$. Three variants of the composition of particles are presented: $H_2O$ ice, the so-called astronomical silicates (their optical characteristics were obtained by synthesizing the results of laboratory and theoretical analysis of details in the IR spectrum in order to ensure agreement with data from a number of astronomical observations), and Mg-Fe silicates (olivines) (labeled as "ice," "sil," and "oli," respectively). The values of their refractive indices change along the spectrum according to Warren and Brandt (2008), Li and Greenberg (1997), and Dorschner et al. (1995), respectively. Details about the reflectance spectra modeling for active asteroids can be found in a paper by Petrova and Busarev (2023).

It is seen from Fig. 4a that the models for nonabsorbing ice and weakly absorbing astronomical silicates differ weakly, while the enhancement in the short-wavelength spectral range naturally increases with the growth of $\tau$, i.e., the number of particles. In contrast to these substances, the absorption in olivines significantly increases at wavelengths shorter than 0.4 μm, which results in suppressing the brightness in the UV range of the spectrum of the exosphere containing these particles (Fig. 4b). The broad size distribution of particles expectedly smooths out spectral details caused by the interference from scattering on particles of close sizes. A model for the ice + olivine mixture (50 to 50% in the number of particles) is also shown. By varying the portion of absorbing particles, it is possible to achieve a slope of the spectrum close to that observed for a specific asteroid, but there is no uniqueness in the estimate of this portion, since the gradient also depends on the number of nonabsorbing particles (Fig. 4a). Nevertheless, a comparison of these model spectra to the spectra measured in a number of asteroids clearly indicates that they are surrounded by a scattering exosphere, where non- (or weakly) absorbing particles with sizes smaller than the wavelength are present.

*Comparison of the Physical and Dynamic Parameters of Active and Inactive Asteroids of Primitive Types*

To find any general differences between active and inactive Main Belt asteroids of primitive types covered by this observational program, we compared their main physical and dynamic parameters, but no differences have been found. There are two possible explanations of this result: (1) there are no noticeable differences at all, since all of the bodies under consideration have approximately the same origin; (2) there are differences, but to detect them, a somewhat statistically more significant sample of objects is needed. To verify the second hypothesis, we compared the distributions of parameters (the semimajor axis of orbits, eccentricity, orbital inclination, and geometric albedo) of the asteroids belonging to two large asteroid families led by 24 Themis (12 288 members) and 145 Adeona (6279 members) (Nesvorný et al., 2015; Novaković et al., 2022) and the largest known asteroids numbered from 1 to 300. Taking into account that we detected the SDA signs on Adeona (C(Ch)-type) and Themis (C(B)-type) (Busarev et al., 2015, 2021), we may suppose that if not all, then the majority of asteroids in both families are of close primitive types, have low-temperature mineralogy, and potentially contain $H_2O$ and $CO_2$ ice reserves in the interior. This comparison revealed that asteroids of the Adeona and Themis families noticeably deviate by the average values of the listed parameters from the corresponding average values obtained for the largest asteroids distributed throughout the entire MAB zone (Fig. 5). The narrow ranges of distributions of the listed parameters for the Themis and Adeona families characterize a close dynamic link between asteroids in each of these families, while close values of their geometric albedo (Fig. 5d) are probably indicative of similarity in the physical and mineralogical properties and, consequently, the *P-T* conditions during the formation of their parent bodies. This is confirmed by very close albedo values, 0.061 and 0.067, for the largest bodies of the families under consideration, Adeona and Themis, respectively (Table 2; https://ssd.jpl.nasa. gov/tools/sbdb_lookup.html#/?sstr=24). However, at the same time, these families show significant differences between the averages of the semimajor axis of the orbit, the orbital inclination, and the eccentricity distribution range (Fig. 5).

Thus based on the above comparison of the distributions of the main dynamic parameters and the geometric albedo of the Themis and Adeona families, we may conclude that, though the geometric albedo values for primitive asteroids of these families are close, the dynamic differences between them are quite large and characterize, probably, their specific dynamic history.

*Analysis of Solar Activity during the Observations of Asteroids*

We also studied the data on solar coronal mass ejections (CMEs) during the period of performing the observation program under discussion; these data were obtained at the SOHO Space Observatory (https://cdaw.gsfc.nasa.gov/CME_list/catalog_description.htm). From December 2021 to the end of February 2022, the overall level of solar activity was relatively low for the most part, but some flares in the X-ray range and associated CMEs occurred. In December 2021 (December 17, 2021), only one halo-type coronal emission covering the full azimuthal angle (up to ~360°) occurred, but its total kinetic energy (TKE) was low. At the expected time of the shock wave passage caused by this CME (at the 2–3 AU heliocentric distances of the asteroids, i.e., approximately 10–12 days after the outburst, taking into account the shock wave propagation in the solar wind plasma with a mean velocity of ~550 km/s (see, e.g., Borovsky, 2020)), only asteroid 859 Bouzaréah was observed (on December 29, 2021; Fig. 3d), which could cause a marked increase in the short-wavelength range of its NRS. In January 2022, four halo-type coronal ejections occurred (their TKE values were at a low level on January 9 and 12, 2022, between low and medium levels on January 14, 2022, and exceeded the medium level on January 29, 2022). However, in January, no asteroid was observed at the moments the solar-wind shockwaves were expected to pass through the MAB zone (Table 3). In February, after the expected CME-induced shockwave had passed through the MAB on January 29, 2022, we observed asteroids 424 Gratia (on February 12, 2022; Fig. 3a), 751 Faina (on February 15, 2022; Fig. 3b), and 778 Theobalda (on February 15, 2022; Fig. 3d). This passage probably caused an increase and noticeable fluctuations in the short- and long-wavelength ranges of the NRSs of these asteroids, which can be seen in the corresponding diagrams. It is interesting to note that no changes were observed in the NRSs of the other asteroids observed on the same nights—398 Admete, 1235 Schorria, 1295 Deflotte, and 1448 Lindbladia, which demonstrated no spectral signatures of SDA either (Table 3). Finally, two halo-type CMEs occurred on the Sun in February (at the low and medium TKE levels on February 11 and 15, 2022, respectively). Shock waves (with low and higher velocities from the first and second CMEs, respectively) from these coronal ejections probably induced ejections of additional amounts of dust from the surface into the exosphere on 762 Pulcova (on 25 February 2022; Fig. 3c) and 859 Bouzaréah (on 25 February 2022; Fig. 3e), which resulted in the enhanced reflectance in the short- and long-wavelength ranges. At the same time, no changes were detected in the NRS of 98 Ianthe, which was observed on the same night and showed no signs of SDA either (Table 3).

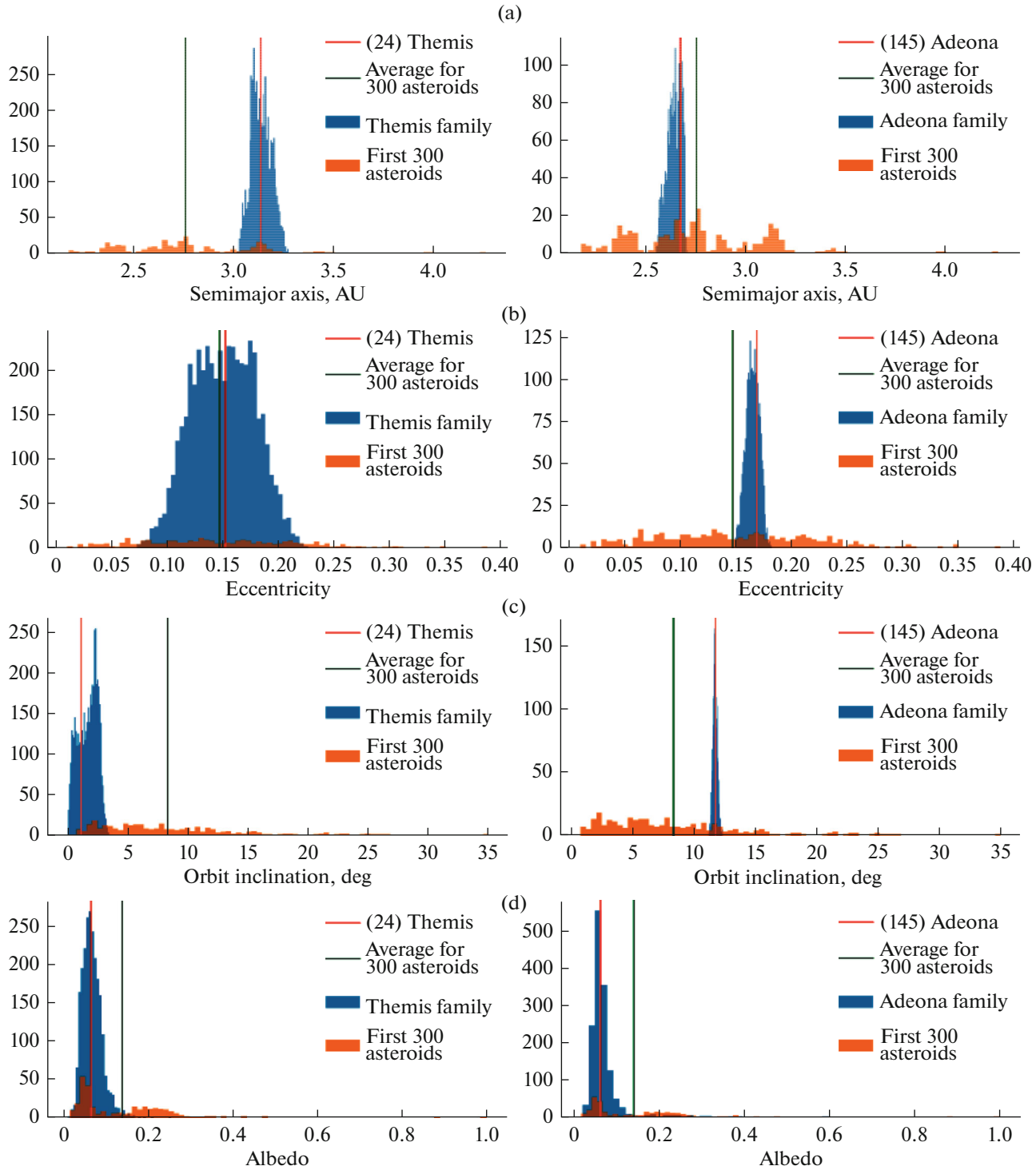


**Fig. 5.** The distributions of the main dynamic parameters and the geomantic albedo values built to compare the asteroids of the Themis (left column of diagrams) and Adeona (right column of diagrams) families and the largest 300 asteroids of the Main Belt (according to https://doi.org/10.26033/6cg5-pt13). The distributions through the semimajor axis of orbits, the eccentricity, the orbit inclination, and the geometric albedo are presented in rows (a)–(d), respectively.

Thus, based on the study of the results of observations, we may conclude that, on the asteroids showing significant (145, 302, 322, 435, 690, and 779) and weaker (424, 751, 762, 778, and 859) signs of activity, SDA was the main process, on which additional effects from the halo-type CME-induced shockwave passages were superimposed and strengthened it. Since the azimuthal coverage of these shockwaves was max-

imal, we may suppose that they reached all the asteroids under consideration.

## DISCUSSION

We note once again that the criteria for including particular Main Belt asteroids into a common observational program were that they are of low-temperature types, have significant orbital eccentricities (at least 0.1), and pass close to the perihelia over a time interval of up to three months. The purpose of the program was to search for objects manifesting SDA under enhanced subsolar temperatures. According to our calculations, for Main Belt asteroids of primitive types with eccentricities of ~0.1–0.3, the difference between the subsolar temperatures at aphelion and perihelion ranges from several tens to hundreds of degrees, depending on specific values of the eccentricity and geometric albedo (Busarev et al., 2018). Obviously, for these asteroids, the main condition of SDA is that they contain ice deposits of $H_2O$ and, with lower probability, $CO_2$. These deposits should be quite close to the surface or even on the surface itself (if these deposits have been recently excavated or there is no upper regolith layer at all, since it was removed at impact events). However, some experts do not allow for even the very possibility of ice layers in the interior of primitive-type asteroids, because there is no direct evidence for this. It is clear that the data of this kind can be obtained only by penetrating the asteroids' interiors by space methods.

As we showed by analytical calculations (Busarev et al., 2003), the concentration of a short-lived isotope $^{26}Al$ (with a half-life period of 0.72 Myr) in Ca–Al inclusions in silicate substance of the early Solar System, which is $^{26}Al/^{27}Al \sim 5 \times 10^{-5}$ (Wasserburg, Papanastassiou, 1982) and corresponds to the analogous quantity in the plane of our Galaxy, $^{26}Al/^{27}Al \sim 10^{-5}$ (Mahoney et al, 1984), was sufficient for accumulating the internal thermal energy, melting completely the ice, and forming an internal water ocean in rock–ice bodies over 200 km in size, which had been formed beyond the $H_2O$ ice formation boundary. An aqueous ocean with a temperature of ~5°C could have persisted on the considered bodies under the 10-km crust for about several million years before complete freezing (Busarev et al., 2003). These results are consistent with those of the other researchers (e.g., Prialnik, Bar-Nun, 1990). The presence of less abundant short-lived isotopes, such as $^{60}Fe$, $^{41}Ca$, $^{10}Be$, etc. (see, e.g., Goswami, 2004), as well as strong impact events on some rock–ice bodies could result in increasing their internal thermal energy and prolonging the lifetime of the ocean. It is important that, taking into account the rates of physical and geochemical processes in the aquatic environment (see, e.g., Veselovsky, 1955), a time period of several million years is sufficient for the substance differentiation (sedimentation) and the formation of layers of hydrated silicates and complex organics.

On the other hand, in accordance with the universal mechanism of the gravitational "sweeping" of small bodies out of the formation zones of major planets, as they reached a scale of several Earths in mass (e.g., Safronov, 1969), it is very likely that such rock–ice bodies were scattered by Jupiter and other giant planets in all directions, as well as into the MAB (Busarev, 2022). These bodies probably became parent bodies of primitive asteroids and could provide delivery of ice and complex organics to the terrestrial planets, including the Earth, rather than only to the MAB (Busarev, 2012; Raymond and Izidoro, 2017; Takir et al., 2023).

That the mentioned processes occurred in the early Solar System is also confirmed by the results of our observations. With the spectrophotometric and *UBVRI* methods, we detected the signs of SDA on 21 asteroids (1, 19, 24, 51, 52, 52, 65, 102, 145, 177, 203, 266, 302, 322, 379, 383, 435, 449, 690, 704, 779, and 1474) of C, B, F, G, and X types (Busarev et al., 2015, 2020, 2021, 2022; Busarev et al, 2016, 2019, 2022; this paper). The spectra agree with the results of numerical simulations of the reflectance spectra of a conditional primitive-type asteroid (with a geometric albedo of 0.07) surrounded by a tenuous exosphere (with an optical thickness <0.5) consisting of aggregates of submicron dust particles of different composition (water ice, olivine, and tholins) (Busarev et al., 2021).

It is also important to note that on 145 Adeona, 302 Clarissa, and 322 Phaeo, which are among the asteroids demonstrating clear signs of activity, as well as in 778 Theobalda, which is suspected of activity, dynamic families of asteroids were found (Table 2; Novaković et al., 2022). This may be interpreted as a consequence of, on average, higher fragility of the ice-containing substance of primitive asteroids, which reveals itself under meteoroid impacts, and, consequently, as an indirect confirmation of the wide occurrence of ice deposits or layers in the asteroids considered. On the other hand, it is obvious that mutual collisions of asteroids in the MAB and strong meteoroid impacts, which cause the destruction of large bodies of primitive composition and the formation of their families, lead to a worse protection of ice deposits on smaller bodies from cosmic factors and their rapid loss.

## CONCLUSIONS

We carried out UBVRI photometric observations (in December 2021 to February 2022) of 29 primitive-type asteroids of the MAB, being near the perihelion distances, and detected spectral signs of quasi-simultaneous SDA on six of these asteroids—145 Adeona, 302 Clarissa, 322 Phaeo, 435 Ella, 690 Wratislavia, and 779 Nina (in 302 Clarissa, 322 Phaeo, 435 Ella, and 690 Wratislavia, for the first time). They amount

to ~21% of the total number of bodies included into this program (or even ~40%, if the bodies with weaker SDA are taken into account). We detected the signs of activity on 145 Adeona and 779 Nina near perihelion (and at a considerable distance from it (Busarev et al., 2015)) for the third time over the last 10 years, which corresponds to about three orbit periods of these asteroids around the Sun. For bodies of similar origin (taking into account their taxonomic types), which were studied under similar observational conditions, these numeric values are significant. These results may be considered as indication of a significant occurrence of $H_2O$ ice in the form of subsurface deposits in primitive-type asteroids of the Main Belt. If this inference is confirmed with more observational material, it will allow us to assert with higher probability that most primitive-type asteroids (or their parent bodies) were formed beyond the $H_2O$ ice line in the early Solar System.

The most significant and widespread physical factors that activate and maintain the ice-sublimation process on primitive-type asteroids are probably a high frequency of impact events in the MAB (including the substance recycling by micrometeoroids), solar-flare and eruptive activity, and an increase in the subsolar temperature of asteroids near perihelion, which facilitates the removal of organic insulating covers formed during ice sublimation and renews the latter process.

It may be supposed that families of asteroids with a large number of members are headed by bodies of primitive composition, which contain ice layers and materials of reduced strength and/or higher fragility. This may be one of the main causes of disintegration of the families' parent bodies by impacts into numerous fragments. At the same time, the smaller bodies in these families should lose the ice component faster due to its worse shielding and thermal insulation.

## FUNDING

The work by V.V. Busarev, E.V. Petrova, M.P. Shcherbina, S.Yu. Kuznetsov, and A.A. Savelova was supported by the Russian Science Foundation (grant no. 22-12-00115).

## OPEN ACCESS



## REFERENCES

Alexander, C.M.O'D., McKeegan, K.D., and Altwegg, K., Water reservoirs in small planetary bodies: Meteorites, asteroids, and comets, *Space Sci. Rev.,* 2018, vol. 214, p. 36.

Bessell, M.S., Standard photometric systems, *Annu. Rev. Astron. Astrophys.,* 2005, vol. 43, pp. 293–336.

Bockelée-Morvan, D., Crovisier, J., Erard, S., Capaccioni, F., Leyrat, C., Filacchione, G., Drossart, P., Encrenaz, T., Biver, N., de Sanctis, M.-C., Schmitt, B., Kuhrt, E., Capria, M.-T., Combes, M., Combi, M., Fougere, N., Arnold, G., Fink, U., Ip, W., Migliorini, A., Piccioni, G., and Tozzi, G., Evolution of $CO_2$, $CH_4$, and OCS abundances relative to $H_2O$ in the coma of comet 67P around perihelion from Rosetta/VIRTIS-H observations, *Mon. Not. R. Astron. Soc.,* 2016, vol. 462 (Suppl. 1), pp. S170–S183. https://doi.org/10.1093/mnras/stw2428

Borovsky, J.E., What magnetospheric and ionospheric researchers should know about the solar wind, *J. Atmosph. Sol.-Terr. Phys,* 2020., vol. 204, p. 105271.

Bradley, A.J., The action of water, in *Meteorites and the Early Solar System II,* Lauretta, D.S. and McSween, H.Y., Jr., Eds., Tucson: Univ. Arizona Press, 2006, pp. 584–624.

Bus, S.J. and Binzel, R.P., Phase II of the Small Main-Belt Asteroid Spectroscopic Survey. The observations, *Icarus,* 2002, vol. 158, pp. 106–145.

Busarev, V.V., Spectrophotometry of atmosphereless celestial bodies of the solar system, *Sol. Syst. Res.,* 1999, vol. 33, pp. 120–129.

Busarev, V.V., A hypothesis on the origin of C-type asteroids and carbonaceous chondrites, *Asteroids, Comets, Meteors (ACM), 2012. Proc. Conf., Niigata, Japan,* May 16–20, 2012, LPI Contrib. 1667, p. 6017. https://arxiv.org/ftp/arxiv/papers/1211/1211.3042.pdf.

Busarev, V.V., Detection of the influence of solar activity on the sublimation activity of primitive asteroids, *Soobshch. konf. "Astronomiya-2018"* (Proc. Conf. "Astronomy-2018"), Obridko, V.N., Ed., Moscow: Trovant, 2018, vol. 2, pp. 47–50.

Busarev, V.V., Active asteroids of the main belt as probable relics of the formation processes of giant planets, *Proc. VAK-2021 Conf. "Astronomy at the epoch of multimessenger studies", SAI MSU, INASAN, Moscow,* 2022, pp. 215–219.

Busarev, V.V., Dorofeeva, V.A., and Makalkin, A.B., Hydrated silicates on Edgeworth–Kuiper objects—probable ways of formation, *Earth, Moon and Planets,* 2003, vol. 92, pp. 345–357.

Busarev, V.V., Barabanov, S.I., Rusakov, V.S., Puzin, V.B., and Kravtsov, V.V., Spectrophotometry of (32) Pomona, (145) Adeona, (704) Interamnia, (779) Nina, (330825) 2008 XE3, and 2012 QG42 and laboratory study of possible analog samples, *Icarus,* 2015, vol. 262, pp. 44–57.

Busarev, V.V., Barabanov, S.I., and Puzin, V.B., Material composition assessment and discovering sublimation activity on asteroids 145 Adeona, 704 Interamnia, 779 Nina, and 1474 Beira, *Sol. Syst. Res.,* 2016, vol. 50, no. 4, pp. 281–293.

Busarev, V.V., Makalkin, A.B., Vilas, F., Barabanov, S.I., and Scherbina, M.P., New candidates for active asteroids: Main-belt (145) Adeona, (704) Interamnia, (779)

Nina, (1474) Beira, and near-Earth (162173) Ryugu, *Icarus,* 2018, vol. 304, pp. 83–94.

Busarev, V.V., Shcherbina, M.P., Barabanov, S.I., Irsmambetova, T.R., Kokhirova, G.I., Khamroev, U.Kh., Khamitov, I.M., Bikmaev, I.F., Gumerov, R.I., Irtuganov, E.N., and Mel'nikov, S.S., Confirmation of the sublimation activity of the primitive main-belt asteroids 779 Nina, 704 Interamnia, and 145 Adeona, as well as its probable spectral signs on 51 Nemausa and 65 Cybele, *Sol. Syst. Res.,* 2019, vol. 53, no. 4, pp. 261–277.

Busarev, V.V., Golubeva, L.F., Petrova, E.V., and Shestopalov, D.I., Variability of the reflectance spectra of (1) Ceres and solar activity, *The Eleventh Moscow Solar System Symposium (11MS3),* October 5–9, 2020, Space Research Inst., Abstract 11MS3-SB-09, pp. 255–258.

Busarev, V.V., Petrova, E.V., Irsmambetova, T.R., Shcherbina, M.P., and Barabanov, S.I., Simultaneous sublimation activity of primitive asteroids including (24) Themis and (449) Hamburga: Spectral signs of an exosphere and the solar activity impact, *Icarus,* 2021, vol. 369, p. 114634.

Busarev, V.V., Shcherbina, M.P., Kuznetsov, S.Yu., Ikonnikova, N.P., and Burlak, M.A., Only a quarter of newly observed primitive asteroids are active, *The Thirteenth Moscow Solar System Symposium (13MS3),* 2022a, Space Research Inst., Abstract 13MS3-SB-01, pp. 244–246.

Busarev, V.V., Savelova, A.A., Shcherbina, M.P., and Barabanov, S.I., Spectral signs of simultaneous sublimation activity and the appearance of a dust exosphere on eight asteroids of the Main belt near perihelion, *Sol. Syst. Res.,* 2022b, vol. 56, no. 2, pp. 84–99.

Chandler, C.O., Curtis, A.M., Mommert, M., Sheppard, S.S., and Trujillo, C.A., SAFARI: Searching asteroids for activity revealing indicators, *Publ. Astron. Soc. Pac.,* 2018, vol. 130, p. 114502.

Dorschner, J., Begemann, B., Henning, T., Jaeger, C., and Mutschke, H., Steps toward interstellar silicate mineralogy. II. study of Mg-Fe-silicate glasses of variable composition, *Astron. Astrophys.,* 1995, vol. 300, pp. 503–520.

Emde, C., Buras-Schnell, R., Kylling, A., Mayer, B., Gasteiger, J., Hamann, U., Kylling, J., Richter, B., Pause, Ch., Dowling, T., and Bugliaro, L., The libRadtran software package for radiative transfer calculations (version 2.0.1), *Geosci. Model Dev.,* 2016, vol. 9, pp. 1647–1672.

Fanale, F.P. and Salvail, J.R., The water regime of asteroid (1) Ceres, *Icarus,* 1989, vol. 82, pp. 97–110.

Gaffey, M.J., Bell, J.F., and Cruikshank, D.P., Reflectance spectroscopy and asteroid surface mineralogy, in *Asteroids II,* Binzel R.P., Gehrels T., and Mattews, M.S., Eds., Tucson: Univ. Arizona Press, 1989, pp. 98–127.

Gaffey, M.J., Cloutis, E.A., Kelley, M.S., and Reed, K.L., Mineralogy of asteroids, in *Asteroids III,* Bottke W.F., Jr., , Eds., Tucson: Univ. Arizona Press, 2002, pp. 183–204.

Goswami, J.N., Short-lived nuclides in the early Solar System: The stellar connection, *New Astron. Rev.,* 2004, vol. 48, pp. 125–132.

Hsieh, H.H., The Hawaii trails project: Comet-hunting in the Main asteroid belt, *Astron. Astrophys.,* 2009, vol. 505, pp. 1297–1310.

Hsieh, H.H. and Haghighipour, N., Potential Jupiter-family comet contamination of the Main asteroid belt, *Icarus,* 2016, vol. 277, pp. 19–38.

Hsieh, H.H. and Jewitt, D.A., Population of comets in the Main asteroid belt, *Science,* 2006, vol. 312, pp. 561–563.

Hsieh, H.H., Novaković, B., Kim, Y., and Brasser, R., Asteroid family associations of active asteroids, *Astron. J.,* 2018, vol. 155, p. 96.

Jewitt, D., The active asteroids, *Astron. J.,* 2012, vol. 143, p. 66.

Jewitt, D. and Hsieh, H.H., The asteroid-comet continuum, in *Comets III,* Meech, K. and Combi, M., Tucson: Univ. Arizona Press, 2022. arXiv preprint arXiv:2203.01397, 2022 [astro-ph.EP].

Kornilov, V., Kornilov, M., Voziakova, O., Shatsky, N., Safonov, B., Gorbunov, I., Potanin, S., Cheryasov, D., and Senik, V., Night-sky brightness and extinction at Mt Shatdzhatmaz, *Mon. Not. R. Astron. Soc.,* 2016, vol. 462, pp. 4464–4472.

Kurucz, R.L., New atlases for solar flux, irradiance, central intensity, and limb intensity, *Mem. Soc. Astron. Italiana,* 2005, vol. 8 Suppl., pp. 189–191.

Li, A. and Greenberg, J.M., A unified model of interstellar dust, *Astron. Astrophys.,* 1997, vol. 232, pp. 566–584.

Longhi, J., Phase equilibria in the system $CO_2$–$H_2O$ I: New equilibrium relations at low temperatures, *Geochim. Cosmochim. Acta,* 2005, vol. 69, pp. 529–539.

Mahoney, W.A., Ling, J.C., Wheaton, Wm.A., and Jacobson, A.S., Discovery of $^{26}$Al in the interstellar medium, *Astrophys. J.,* 1984, vol. 286, pp. 578–585.

McSween, H.Y., Jr., Ghosh, A., Grimm, R.E., Wilson, L., and Young, E.D., Thermal evolution models of asteroids, in *Asteroids III,* Bottke, W.F., Jr., , Eds., Tucson: Univ. Arizona Press, 2002, pp. 559–571.

Mironov, A.V., *Osnovy astrofotometrii. Prakticheskie osnovy vysokotochnoi fotometrii i spektrofotometrii zvezd* (Fundamentals of Astrophotometry. Practical Fundamentals of High-Precision Photometry and Spectrophotometry of Stars), Moscow: Fizmatlit, 2008.

Nesvorný, D., Brož, M., and Carruba, V., Identification and dynamical properties of asteroid families, in *Asteroids IV,* Bottke, W.F., DeMeo, F.E., and Michel, P., Eds., Tucson: Univ. Arizona Press, 2015, vol. 29, pp. 297–321.

Novaković, B., Vokrouhlický, D., Spoto, F., and Nesvorný, D., Asteroid families: Properties, recent advances, and future opportunities, *Celestial Mech. Dyn. Astron.,* 2022, vol. 134, no. 4, p. 34. http://asteroids.matf.bg.ac.rs/fam/familymembers.php.

Petrova, E.V. and Busarev, V.V., On the prospects for estimating the properties of particles in an active asteroid exosphere by features in the UV and visible reflectance spectra, *Sol. Syst. Res.,* 2023, vol. 57, no. 2, pp. 161–174.
https://doi.org/10.1134/S0038094623020065

Prialnik, D. and Bar-Nun, A., Heating and melting of small icy satellites by the decay of $^{26}$Al, *Astrophys. J.,* 1990, vol. 355, pp. 281–286.

Raymond, S.N. and Izidoro, A., Origin of water in the inner Solar System: Planetesimals scattered inward during

Jupiter and Saturn's rapid gas accretion, *Icarus,* 2017, vol. 297, pp. 134–148.

Safronov, V.S., *Evolyutsiya doplanetnogo oblaka i obrazovanie Zemli i planet* (Evolution of the Pre-planetary Cloud and the Formation of the Earth and Planets), Moscow: Nauka, 1969.

Sanchez, J.A., Reddy, V., Nathues, A., Cloutis, E.A., Mann, P., and Hiesinger, H., Phase reddening on near-Earth asteroids: Implications for mineralogical analysis, space weathering and taxonomic classification, *Icarus,* 2012, vol. 220, pp. 36–50.

Schorghofer, N., The lifetime of ice on main belt asteroids, *Astrophys. J.,* 2008, vol. 682, pp. 697–705.

Schorghofer, N., Predictions of depth-to-ice on asteroids based on an asynchronous model of temperature, impact stirring, and ice loss, *Icarus,* 2016, vol. 276, pp. 88–95.

Shustov, B.M., Zolotarev, R.V., Busarev, V.V., and Shcherbina, M.P., Impact events as a possible mechanism to initiate sublimation–dust activity of main-belt asteroids, *Astron. Rep.,* 2022, vol. 66, pp. 1098–1110.

Sugita, S., Honda, R., Morota, T., Kameda, S., Sawada, H., Tatsumi, E., and 117 co-authors, The geomorphology, color, and thermal properties of Ryugu: Implications for parent-body processes, *Science,* 2019, vol. 364, p. eaaw0422.

Sykes, M.V., Greenberg, R., Dermott, S.F., Nicholson, P.D., and Burns, J.A., Dust bands in the asteroid belt, in *Asteroids II,* Binzel, R.P., Gehrels, T., and Mattews, M.S., Eds., Tucson: Univ. Arizona Press, 1989, pp. 336–367.

Takir, D., Neumann, W., Raymond, S.N., Emery, J.P., and Trieloff, M., Late accretion of Ceres-like asteroids and their implantation into the outer main belt, *Nat. Astron.,* 2023. https://doi.org/10.1038/s41550-023-01898-x

Tholen, D.J., Asteroid taxonomic classifications, in *Asteroids II,* Binzel, R.P., Gehrels, T., and Mattews, M.S., Eds., Tucson: Univ. Arizona Press, 1989, pp. 1139–1150.

Tholen, D.J. and Barucci, M.A., Asteroid taxonomy, in *Asteroids II,* Binzel, R.P., Gehrels, T., and Mattews, M.S., Eds., Tucson: Univ. Arizona Press, 1989, pp. 298–315.

Veeder, G.J. and Tedesco, E.F., *Results from the IRAS Minor Planet Survey, The IRAS Minor Planet Survey. Final Report PL-TR-92-2049,* Tedesco, E.F., , Eds., Massachusetts: Phillips Laboratory, 1992, pp. 107–126.

Veselovskii, V.S., *Khimicheskaya priroda goryuchikh iskopaemykh* (Chemical Nature of Fossil Fuels), Moscow: Inst. Gornogo Dela. Izd. Akad. Nauk SSSR, 1955.

Warren, S.G. and Brandt, R.E., Optical constants of ice from the ultraviolet to the microwave: A revised compilation, *J. Geophys. Res.*, 2008, vol. 113, p. D14220. https://doi.org/10.1029/2007JD009744

Wasserburg, G.J. and Papanastassiou, D.A., Some short-lived nuclides in the early Solar System—A connection with the placental ISM, in *Essays in Nuclear Astrophysics,* Barnes, C.A., Clayton, D.D., Schramm, D.N., Eds., Cambridge: Cambridge Univ. Press, 1982.

Zolensky, M.E., Bourcier, W.L., and Gooding, J.L., Aqueous alteration on the hydrous asteroids: Results of EQ3/6 computer simulations, *Icarus,* 1989, vol. 78, pp. 411–425.

*Translated by E. Petrova*